

Validity of the dipole approximation in TEM-EELS studies

R.F. Egerton¹, R.A. McLeod^{1,2} and M. Malac^{1,2}

¹Physics Department, University of Alberta, Edmonton, Canada T6G 2E1

²National Institute for Nanotechnology, Edmonton, Canada T6G 2M9

KEYWORDS EELS; non-dipole; Lorentzian angular distribution

ABSTRACT Non-dipole effects in electron energy-loss spectroscopy are evaluated in terms of deviation of the inelastic scattering from a Lorentzian angular dependence, which is assumed in established procedures for plural-scattering deconvolution, thickness measurement and Kramers-Kronig analysis. The deviation appears to be small and may be outweighed by the effect of plural (elastic + inelastic) scattering, which is not removed by conventional deconvolution methods.

In the core-loss region of the spectrum, non-Lorentzian behaviour stems from reduction of the generalized oscillator strength from its optical value and (for energies far above an ionization threshold) formation of a Bethe-ridge angular distribution. At incident energies above 200 keV, retardation effects further distort the angular distribution, even for core losses just above threshold.

With an on-axis collection aperture, non-dipole effects are masked by the rapid falloff of intensity with scattering angle, but they may be important for off-axis measurements. Near-edge fine structure is sensitive to non-dipole effects but these can be minimized by use of an angle-limiting collection aperture.

INTRODUCTION

At the accelerating voltages used in the TEM and STEM, the inelastic scattering of a transmitted electron is predominantly a dipolar interaction (just as in optical excitation), leading to a Lorentzian angular distribution of the inelastic signal S per unit solid angle:

$$dS/d\Omega = C/(\theta^2 + \theta_E^2) \quad (1)$$

where C is a constant, θ is the scattering angle and θ_E is the characteristic angle for an energy loss E , given by E/mv^2 (m = relativistic electron mass, v = incident-electron speed) or approximately $E/(2E_0)$ at small incident energy E_0 . This dipole formalism allows scattering cross sections and sum rules to be written using relatively simple equations that form the basis of various spectral-processing procedures such as Kramers-Kronig analysis, quantitative elemental analysis and the measurement of specimen

thickness. Equation (1) is also assumed when correcting for plural inelastic scattering and incident-beam angular convergence, as discussed below.

In practice, the dipole approximation holds only over a limited angular range. As the scattering angle approaches some value θ_c , the scattered intensity falls off more rapidly than implied by Eq. (1), equivalent to reduction in the coefficient C . For scattering that involves single-electron excitation, this critical angle is often taken as the Bethe-ridge angle: $\theta_c \sim (E/E_0)^{1/2}$ (Inokuti, 1971). For plasmon scattering, a Hartree-Fock calculation (Ferrell, 1957) gives $\theta_c \sim (0.74)E_p/(p_0v_F)$, where p_0 is the incident-electron momentum and v_F is the magnitude of the Fermi velocity, in agreement with 300kV measurements on a 100nm polycrystalline Al film (Bertoni et al., 2011). In many materials, the two formulas for θ_c give similar values; see Table 1.

Although θ_c is often described as a cutoff angle, the cutoff of intensity is only gradual. There is always some single-electron scattering above θ_c , even in free-electron plasmon metals such as Al (Batson and Silcox, 1983).

To ensure validity of the dipole formalism, it therefore seems necessary to restrict the collection semi-angle β of the electron spectrometer to a value less than θ_c . For low energy losses, the angles involved are then quite small (see Table 1) and choosing $\beta \ll \theta_c$ reduces the energy-loss signal and the signal/noise ratio. More importantly, Eq.(1) assumes parallel illumination, whereas the convergence semi-angle α of a focused electron probe can easily exceed θ_c , especially for very small probes formed by aberration-corrected lenses. In this situation, a small collection aperture greatly reduces the inelastic signal without selecting scattering angles smaller than θ_c .

Table 1: characteristic and cutoff angles (in mrad) for $E_0 = 100$ keV and $v_F = 10^6$ m/s.

E(eV)	θ_E (mrad)	$(E/E_0)^{1/2}$	$0.74E/(p_0v_f)$
10	0.054	10	7
30	0.16	17	20
100	0.54	32	--
300	1.6	57	--

QUANTITATIVE ANALYSIS OF LOW-LOSS SPECTRA

The low-loss region of the energy-loss spectrum is usually understood to imply energy losses below about 100 eV. In this region, inelastic scattering involves mainly outer-shell (valence or conduction) electrons and gives rise to plasmon excitation. The average distance between scattering events (the inelastic or plasmon mean free path) lies

within the range 50 nm to 200 nm, depending on the incident energy and the chemical composition of the specimen. Often the thickness of the TEM specimen is also within this range, so plural scattering (where a transmitted electron undergoes more than one scattering event) is unavoidable. Because plural scattering invalidates the use of a single-scattering formula, it is often removed (in a process referred to as deconvolution) as the first step in spectral processing.

The most common deconvolution procedures are the Fourier-log method (which can be applied to the entire spectrum) and Fourier-ratio processing (used to remove plasmon/core-loss scattering from ionization edges). These procedures are exact only if all scattering is recorded, implying a large collection aperture β but in contradiction with the dipole requirement above. It can be shown that the error introduced by using a small aperture is minor, thanks to the θ^{-2} behaviour of the Lorentzian angular distribution for $\theta \gg \theta_E$ (Egerton and Wang, 1990; Su et al., 1992; Egerton and Wong, 1995). As a result, deconvolution routines perform adequately provided $\beta \gg \theta_E$, as is usually the case (see Table 1; β is typically 5 mrad or more).

Provided the energy-loss spectrum has been recorded with an on-axis angle-limiting aperture (e.g. TEM objective aperture) that accepts electrons scattered through angles up to β , integration of Eq.(1) gives the single-scattering inelastic intensity as:

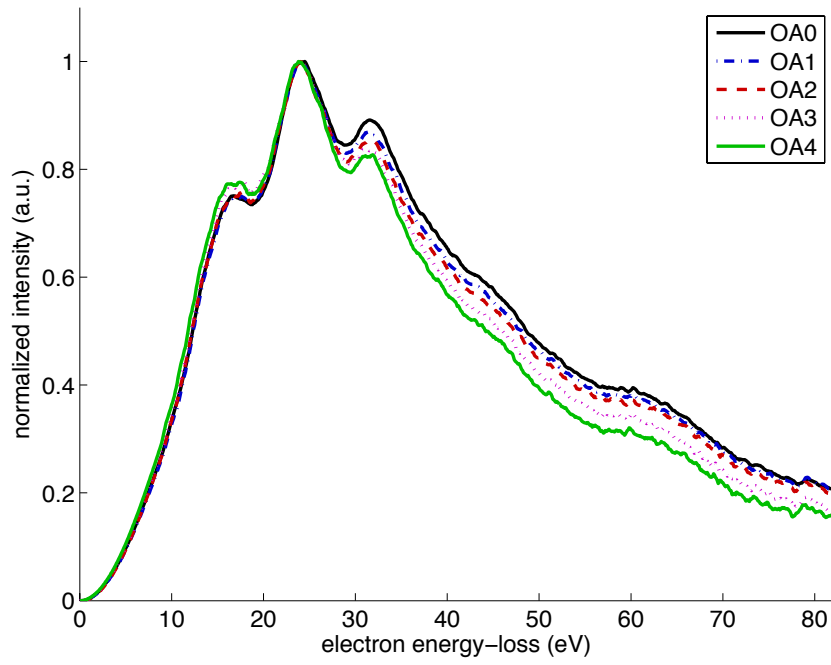
$$S(E) = I_0 t (2\pi a_0 T)^{-1} \text{Im}[-1/\epsilon(E)] \log_e(1+\beta^2/\theta_E^2) \quad (2)$$

where I_0 is the integral of the zero-loss peak, t is the specimen thickness, $a_0 = 52$ pm, and $T = m_0 v^2/2$ (somewhat less than the incident energy E_0 because the relativistic mass m of an incident electron exceeds its rest mass m_0). $\text{Im}[-1/\epsilon(E)]$ is the so-called energy-loss function, $\epsilon(E)$ being the complex relative permittivity for a photon frequency $f = E/h$, where h is the Planck constant.

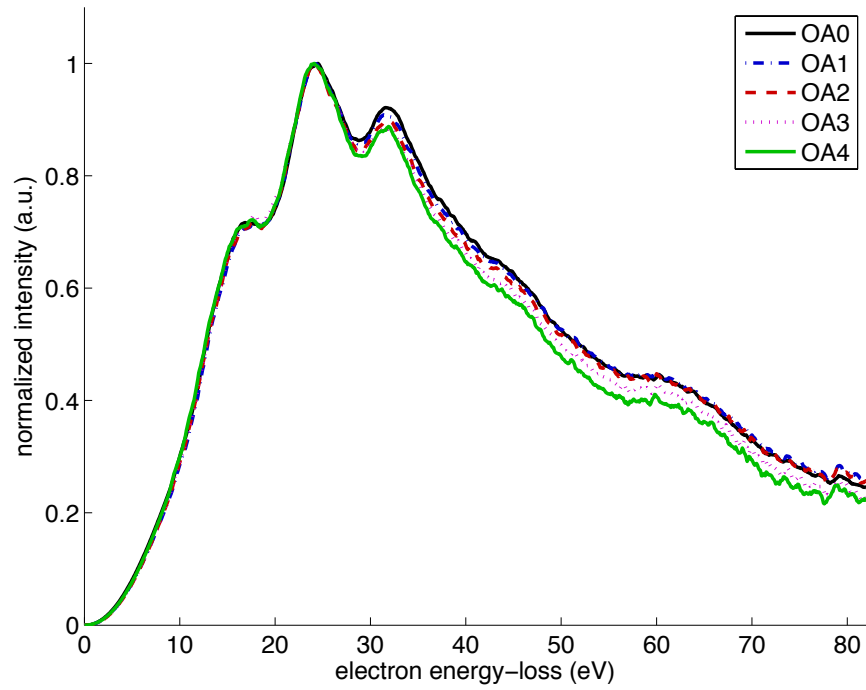
Figure 1a shows low-loss spectra recorded from a gold film, each corrected (by Fourier-log deconvolution) for plural inelastic scattering. The spectra correspond to collection semi-angles between 2.6 mrad (smallest TEM objective aperture) and 104 mrad (no objective aperture). Their intensities are expected to differ because of the different values of the aperture function, $\log_e(1+\beta^2/\theta_E^2)$ in Eq.(2).

According to Eq.(2), these differences can be removed by applying a standard ‘‘aperture correction’’: dividing each data point by $\log_e(1+\beta^2/\theta_E^2)$ where θ_E varies with energy loss but β is a constant, determined by the collection-aperture radius. As shown in Fig. 1b, however, some difference among the spectra still remains. Recognizing that the cutoff angle $\theta_c \sim (E/E_0)^{1/2}$ can be less than β at low energy loss, it seems appropriate to replace β by $(E/E_0)^{1/2}$ in Eq.(2) whenever $(E/E_0)^{1/2} < \beta$. After applying this revised form of correction, the energy dependences lie within a few percent of each other; see Fig. 1c. Similar results (not shown) were obtained from data recorded from a silicon specimen using 100keV electrons.

(a)



(b)



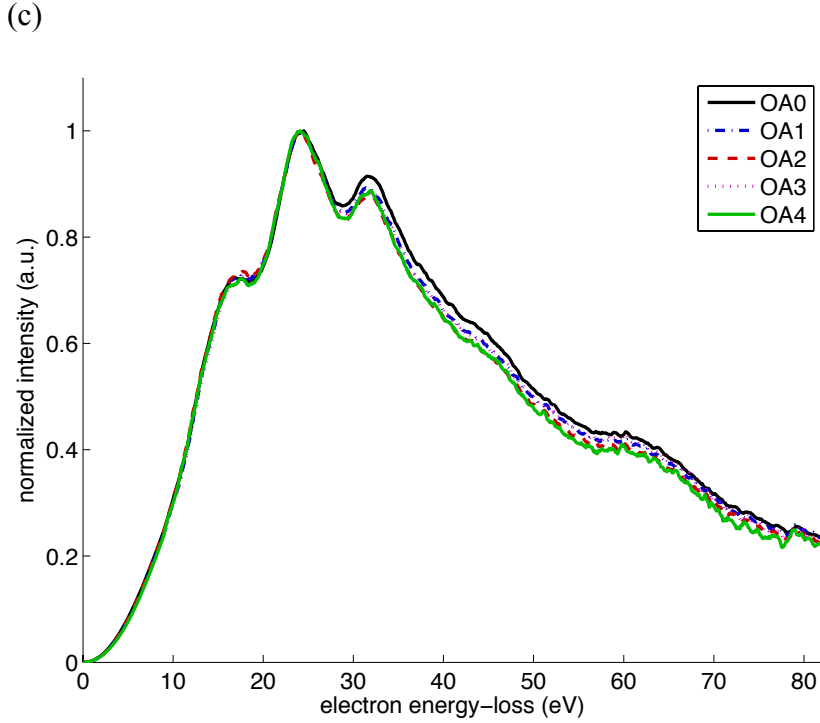


Fig.1. (a) Low-loss spectra recorded from a gold film with $E_0 = 300$ keV and different collection apertures: $\beta = 104$ mrad (OA0), 18 mrad (OA1), 12 mrad (OA2), 4.6 mrad (OA3) and 2.6 mrad (OA4). (b) Same spectra after dividing by the aperture function $\log_e(1+\beta^2/\theta_E^2)$. (c) Same spectra after dividing by $\log_e(1+\beta^2/\theta_E^2)$ with β taken as $(E/E_0)^{1/2}$ whenever $(E/E_0)^{1/2} < \beta$. All spectra have been normalized at the plasmon maximum.

Low-loss spectra can be used to measure the local thickness of a TEM specimen. One method for doing this makes use of a Kramers-Kronig sum rule, according to which the thickness t is given by:

$$t = (4a_0T/I_0) (1-1/n^2)^{-1} \int [S(E)/E] [\log_e(1+\beta^2/\theta_E^2)]^{-1} dE \quad (3)$$

where n is the refractive index of the specimen at optical frequencies. For a metal or good conductor, n is large and $1/n^2$ can be taken as zero. The procedure described by Eq.(3) is a standard item in the EELS menu of the Gatan company's Digital Micrograph spectrum-processing software. The form of the logarithm term in Eq.(3) implies that dipole scattering predominates.

Figure 2 shows measurements of the thickness of a gold film, based on Eq.(3) with five value of β . Because Eq.(3) assumes the dipole scattering, it is expected to fail for larger collection semi-angles. Indeed, the measured thickness falls from about 68 nm at $\beta = 2.6$ mrad to 50 nm at $\beta = 18$ mrad, then to below 40 nm for $\beta = 104$ mrad where a dipole formula is clearly inappropriate. Limiting the value of β in the formula to 12.9 mrad (the Bethe-ridge cut-off for $E = 50$ eV) reduces the t -variation at high β (dashed

black line in Fig.2), as might be expected. Implementation of the previous scheme, in which β is replaced by $\theta_c = (E/E_0)^{1/2}$ where necessary, further reduces the variation but leaves a 15% variation in measured thickness over the entire angular range (red dash-dot curve in Fig. 2).

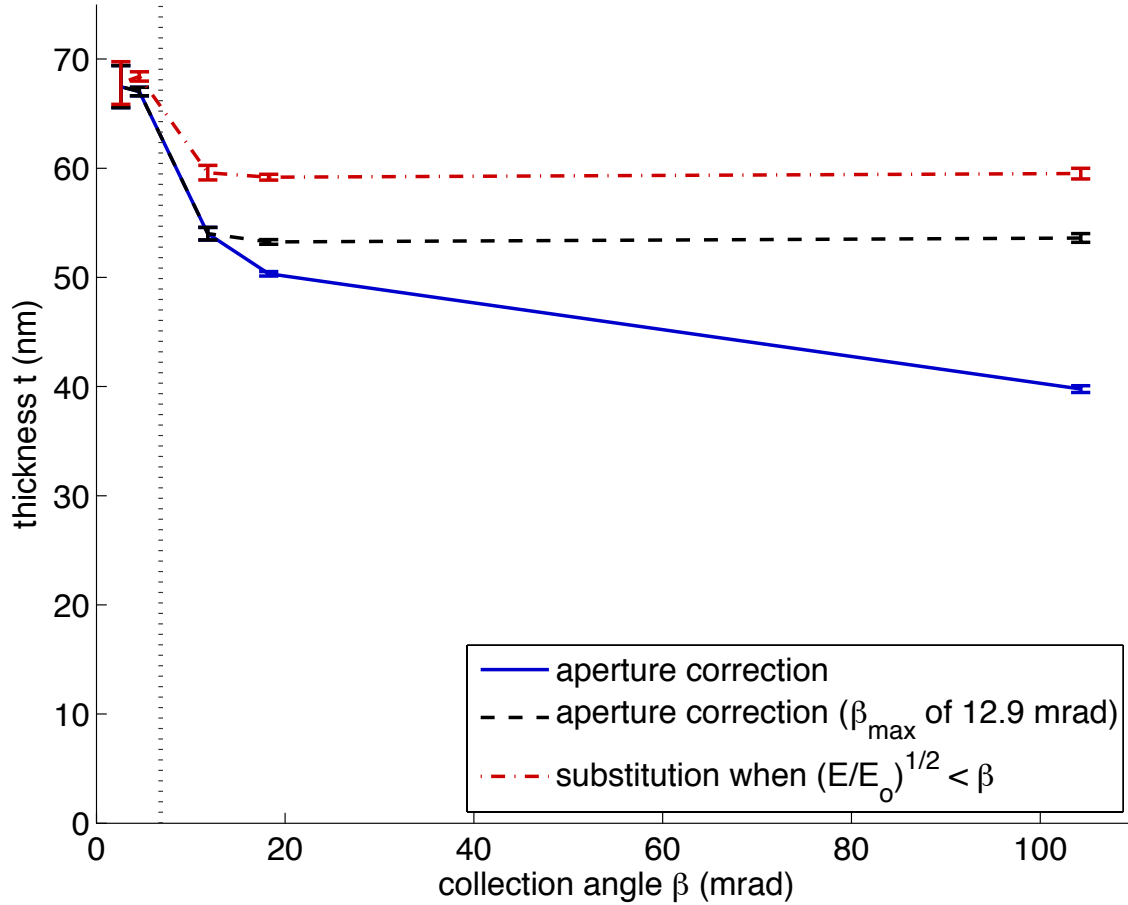


Fig. 2. Thickness measurements on a gold film using 300keV incident electrons and different collection semi-angles. Error bars show the variation in measured thickness between nearby areas of film. The dotted vertical line shows the value of the lowest-order Bragg-scattering angle θ_c .

Having attempted to allow for the angular cutoff, we might presume that the remaining variation seen in Fig. 2 stems from other factors. Especially in thicker specimens, the angular distribution of inelastic scattering is affected by the simultaneous occurrence of elastic scattering. In the case of a crystalline specimen, this elastic scattering takes the form of Bragg beams, each of which can act as a secondary source of inelastic scattering. In the kinematic (thin-specimen) limit, where Bragg intensities are weak and there is little chance of an electron being re-scattered into the central beam, each Bragg beam is simply broadened by the inelastic scattering, whose the angular distribution can be assumed to be described by Eq.(1).

On average, elastic scattering involves much larger angles than inelastic scattering. Each Bragg beam corresponds to scattering angle $\theta_e = \lambda/d$, where d is the interplanar spacing and λ is the transmitted-electron wavelength. For gold and 300keV electrons ($\lambda = 1.97$ pm), the lowest value of θ_e is 7 mrad, a value less than the critical angle for inelastic scattering (Table 1). Some of the Bragg-beam electrons will therefore be scattered inelastically back towards the optic axis so that they enter a small on-axis collection aperture. A larger aperture should increase this Bragg-beam contribution, which may account for the initial rise in t in Fig.2. But when $\beta > \theta_e$, Bragg-beam electrons start to contribute to I_0 in Eq.(3), giving a decrease in the measured thickness, as in Fig.2. Our suggested explanation for the 15% thickness variation in Fig. 2 is therefore in terms of plural (elastic + inelastic) scattering, an effect not included in Eq. (3) and not removed by the usual inelastic-scattering deconvolution.

Bertoni et al. (2011) divided Fourier transforms of plasmon-loss and zero-loss diffraction patterns recorded from a 100nm film of polycrystalline Al using 300keV electrons. This two-dimensional Fourier-ratio deconvolution was apparently successful in correcting for Bragg+plasmon scattering, since it resulted in the expected single-scattering angular distribution of plasmon scattering. But elastic and phonon scattering is strong in materials of high atomic number such as gold and, except in ultra-thin specimens, the scattering is dynamical. It is then unlikely that 2-D Fourier-ratio deconvolution will be accurate and a more elaborate scheme (e.g. Batson and Silcox, 1983) may be necessary.

Another application of low-loss EELS is for determining the local bandgap E_g in a semiconductor or insulator, E_g being taken as the energy loss at which inelastic scattering (causing conduction electrons to be excited to an empty valence band) starts to appear. Apart from the tail of the zero-loss peak, the main problem here is an inelastic background caused by Cerenkov emission, which occurs if the electron travels faster than the speed of light (c/n) within the specimen. Cerenkov loss is characterized by a narrow angular distribution that is distinctly non-Lorentzian: the inelastic intensity typically peaks at an angle of several microradians (Stoeger-Pollach et al., 2006). Its energy-dependence is complicated by the occurrence of surface-plasmon modes, whose intensity also has a non-Lorentzian angular dependence, peaking at $\theta_E/3^{1/2}$ in the case of a thicker specimen and decreasing as θ^3 at higher angles.

Some monochromated TEM-EELS systems now achieve an energy resolution below 20 meV, sufficient to investigate nuclear-vibrational (phonon) modes of energy loss (Krivanek et al, 2013). At small scattering angles, the phonon signal is dominated by dipole scattering, with a narrow Lorentzian angular distribution that implies a spatial resolution limited to some tens of nm (Egerton, 2014). At higher angles, there appears to be a non-dipole component, which may offer the possibility of high spatial resolution in radiation-resistant specimens (Cueva and Muller, 2013; Dwyer, 2014; Rez, 2014).

QUANTITATIVE ANALYSIS OF CORE-LOSS SPECTRA

At energy losses above 100 eV, inner-shell (atomic-core) excitation gives rise to ionization edges whose threshold energy is approximately the binding energy of a particular inner shell. Inner-shell excitation being an atomic rather than collective effect, the single-scattering core-loss intensity is usually written in terms of an energy-differential oscillator strength per atom df/dE , rather than the energy-loss function:

$$S_c(E) = I_0 (n_a t) 4\pi a_0^2 (R/T)(R/E) (df/dE) \log_e(1+\beta^2/\theta_E^2) \quad (4)$$

where n_a is the concentration (atoms/volume) of the element giving rise to the edge and R is the Rydberg energy (13.6 eV). At low scattering angles, df/dE is constant and equal to the optical oscillator strength, which effectively defines the dipole region of scattering.

Equation (4) can be integrated over an energy range Δ beyond the edge threshold, to provide a formula that is useful for elemental analysis. If deconvolution is employed to remove plural (plasmon + core-loss) scattering, the core-loss integral is given by:

$$I_c(\beta, \Delta) = I_0 (n_a t) \sigma_c(\beta, \Delta) \quad (5)$$

Applying Eq.(5) to the ionization edges of two different elements, the concentration ratio is obtained from a measured ratio of core-loss intensities and a ratio of calculated cross sections, without any need to know the zero-loss integral I_0 or the specimen thickness t . Software is available for calculating each core-loss cross section $\sigma_c(\beta, \Delta)$ without making a dipole approximation (Egerton, 1978; Leapman et al, 1980)..

However, concerns about the effect of elastic scattering are even more relevant to the core-loss region. Because $\theta_E = E/mv^2$ increases with energy loss E , there is a reasonable probability of an elastically scattered electron being core-loss scattered back into the collection aperture (or vice versa), increasing the value of $I_c(\beta, \Delta)$ above that given by Eq. (5). For an amorphous specimen, this probability increases with increasing specimen thickness but decreases with increasing aperture size; for $\beta \sim 20$ mrad it should be less than 10% for specimens up to 100nm thick (Cheng and Egerton, 1993; Egerton and Wong, 1995). In a crystalline specimen, the effect of elastic scattering depends on the Bragg angles relative to the aperture semi-angle and (for a single crystal) on the specimen orientation and thickness. Allowing for dynamical effects and phonon scattering, the resulting core-loss intensity can be calculated down to the atomic scale (Urban et al., 2013) but only if the crystallographic structure and composition of the specimen are already known.

Just as for the low-loss region, we can examine non-dipole effects in terms of the extent to which the angular distribution of inelastic scattering departs from the Lorentzian form that gives rise to Eq.(4). Figure 3 shows predictions of the K-loss intensity collected by an on-axis aperture, based on a hydrogenic model (Egerton, 1978). At the oxygen K-edge threshold and at an energy 100 eV above the threshold, the intensity starts to fall below the Lorentzian prediction for $\theta > 20$ mrad, reflecting a decrease in the oscillator strength below its optical value. For an energy 500 eV beyond the edge, however, a Lorentzian formula *underestimates* the intensity at higher collection angles and the angle-

integrated intensity. This underestimate arises because, for energy losses greatly exceeding the binding energy of the electrons being excited, these electrons behave more like free particles. The angular distribution of inelastic scattering changes from having its maximum at $\theta = 0$ (as for the Lorentzian angular distribution) to a maximum around the Bethe-ridge angle $\theta = (E/E_0)^{1/2}$. This situation occurs also in the case of valence-electron scattering, which can be a major component to the background preceding an ionization edge, in which case a small collection angle is needed to maximize the edge/background ratio (Egerton, 2011).

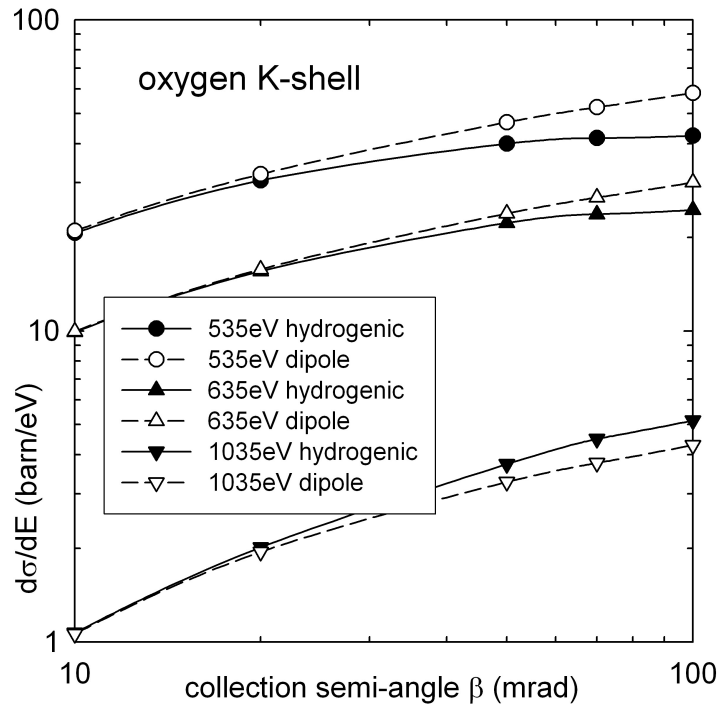


Fig. 3. Oxygen K-shell intensity (at 535 eV, 635 eV and 1035 eV) collected by an aperture of semi-angle β , as calculated using a hydrogenic model and as predicted by a dipole formula, Eq. (2).

For the L_{23} edges of some elements (e.g. Al, Si, certain transition metals), as well as the M_{45} edges of some rare earths, the spectral intensity is suppressed at energy losses just above the ionization threshold by a “centrifugal” potential barrier within each atom, giving rise to a rounded edge with a “delayed maximum” (Leapman et al., 1980). This effect alters the angular distribution of core-loss scattering but is not very significant since it occurs mainly within 10 eV of the threshold, where the intensity is low (Manson, 1972).

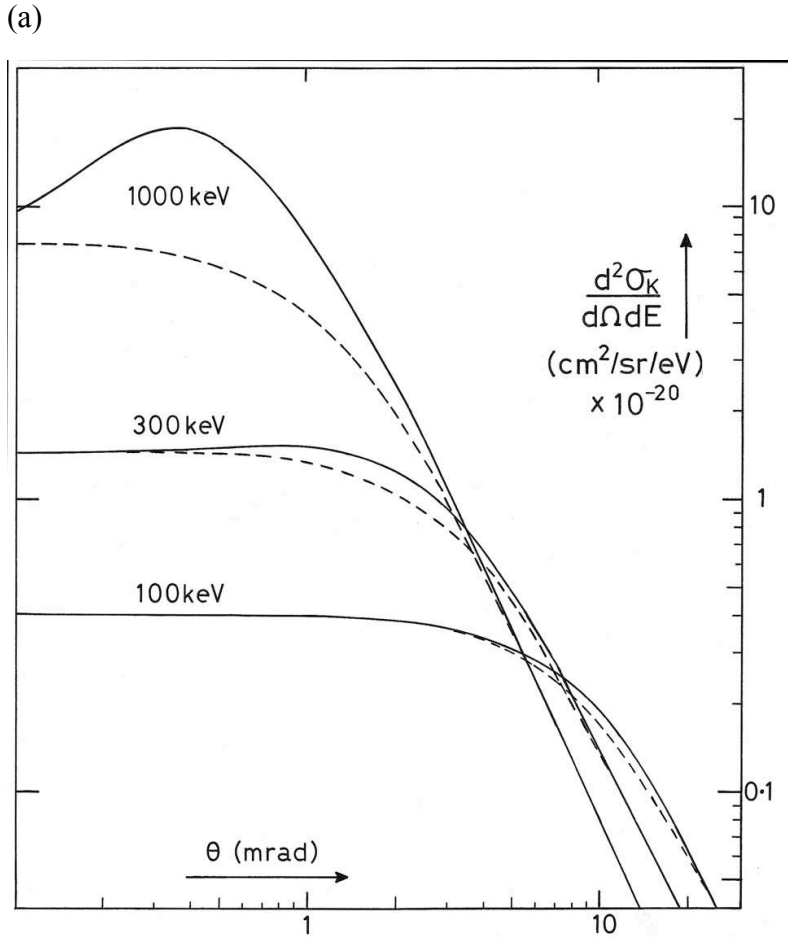
Loeffler et al. (2011) measured small departures from a Lorentzian angular distribution as the EELS collection aperture was moved off-axis to record higher-angle L-shell scattering of 200keV electrons in silicon. The rapid fall in intensity gave rise to

dynamic-range and statistical-noise problems; to reduce such problems, they recorded also the variation of L-shell intensity with energy loss (between 100 eV and 200 eV) for a spectrometer entrance aperture 7.8 mrad away from the optic axis. The intensity just above threshold was found to be up to 25% smaller than a Lorentzian prediction.

Another situation in which the angular distribution of core-loss scattering becomes non-Lorentzian is at high incident energies. When an incident electrons travels close to the speed of light, relativistic retardation effects occur and Cerenkov x-rays can be emitted (Bazylev et al., 1976). The core-loss angular distribution is broadened and $dS/d\Omega$ peaks at a non-zero angle, as shown in Fig. 5a. This effect has been confirmed by energy-filtered diffraction measurements on amorphous carbon at $E_0 = 1$ MeV (Kurata et al., 1997). Retardation augments the logarithm term in Eq.(4) by an amount (Egerton, 2011):

$$G = 2\log_e\gamma - \log_e[(\beta^2 + \theta_E^2)/(\beta^2 + \theta_E^2/\gamma^2)] - (v^2/c^2)[\beta^2/(\beta^2 + \theta_E^2/\gamma^2)] \quad (6)$$

where $\gamma = 1 - v^2/c^2$. At $E_0 = 300$ keV, the angle-integrated cross section is increased by about 20% for collection semi-angles of the order of the characteristic angle θ_E , as seen in Fig. 5b.



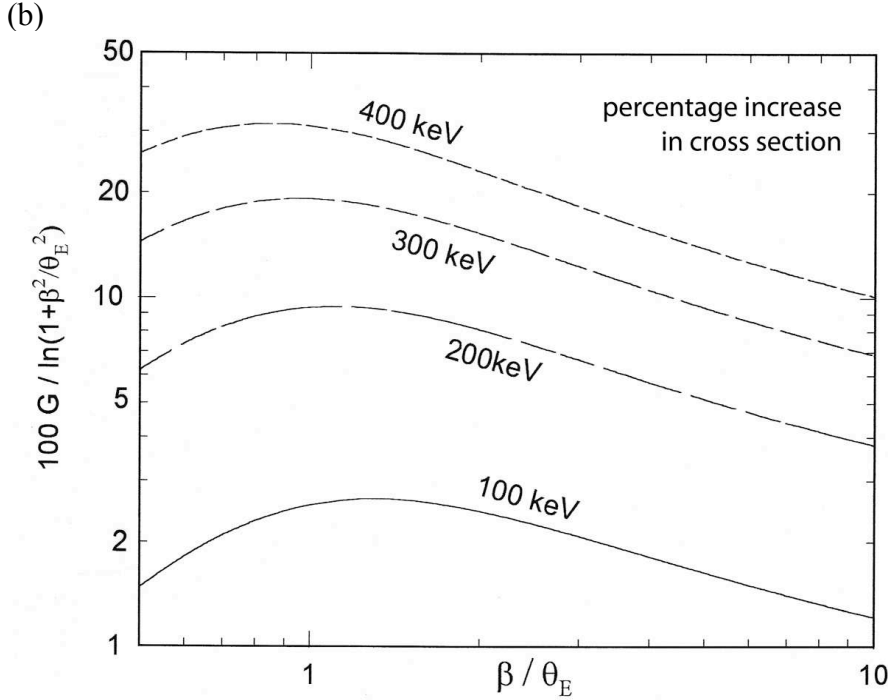


Fig. 5. (a) Energy-differential cross section (energy loss just above the ionization threshold) for K-shell scattering, calculated for an Al atom using a hydrogenic model with (solid curves) and without (dashed curves) relativistic retardation. (b) Percentage increase (due to retardation) in the angle-integrated cross section, according to Eq.(6), plotted as a function of the normalized collection semi-angle β .

In the case of an anisotropic material such as graphite, the situation is more complicated. For a uniaxial material such as graphite, the σ^* and π^* intensities depend on specimen orientation relative to the incident beam (Souche et al., 1998; Radtke et al., 2006) but the total intensity is independent of orientation and has an angular dependence similar to Fig.5a.

Besides their use for elemental quantification, ionization edges are of interest because their fine structure gives an indication of the electronic band structure and the density ρ_f of unoccupied states above the Fermi level. According to the Fermi Golden Rule, the probability P_{if} for electron transition from an initial atomic state Ψ_i to a continuum final state Ψ_f is

$$P_{if} = (1/h) |M_{if}|^2 \rho_f \quad (7)$$

where the matrix element $M_{if} = \int \Psi_f^* \exp(i\mathbf{q}\cdot\mathbf{r}) \Psi_i$ is a property of the atom involved and \mathbf{q} is the scattering wavevector. Dipole transitions correspond to the first term $i(\mathbf{q}\cdot\mathbf{r})$ in the expansion of the $\exp(i\mathbf{q}\cdot\mathbf{r})$ operator; higher-order non-dipole terms are small provided $q \ll 1/r_c$, where r_c is the radius of the core state. A hydrogenic model gives $r_c = a_0/Z^*$, the effective nuclear charge Z^* being related to atomic number Z by $Z^* = Z - 0.3$ for a K-shell initial state (Egerton, 1978). Therefore dipole conditions should hold for $\theta \ll$

$Z^*/(k_0 a_0)$, implying $\theta \ll 63$ mrad for the carbon K-edge and 100keV electrons ($k_0 = 1697/\text{nm}$). For the carbon-K and Ti-L₂₃ edges, Rez (1989) calculated that non-dipole components amount to less than 10% for $q < 45 \text{ nm}^{-1}$ ($\theta < 23$ mrad for 100keV electrons). If a large (100mrad) collection aperture is used, dipole-forbidden transitions can become weakly visible; for example, lanthanum M₂ and M₃ edges from La₂O₃, which disappear when a small (1.6mrad) aperture is used (Ahn and Krivanek, 1983).

Saldin and Yao (1990) calculated that the non-dipole contribution becomes substantial at energies well above the ionization threshold: 270 eV above threshold for the oxygen K-edge. Essex et al. (1999) concluded that the dipole approximation is inappropriate beyond 50 eV for Li K-edge atomic imaging. In the near-edge region, however, the dipole selection rule can be expected to hold: K-shell spectroscopy with a collection semi-angle below 20 mrad will measure mainly the density of empty p-states, while L-shell analysis will measure mainly d-states.

CONCLUSIONS

Modern TEMs are capable of analyzing very small areas of specimen but this capability may involve focusing the electrons into a small-diameter probe whose angular convergence exceeds the dipole range of scattering. The validity of EELS formulas that incorporate the dipole approximation is therefore of concern.

We have investigated non-dipole effects in terms of departure of the angular distribution of inelastic scattering from a Lorentzian dependence. For energy losses below 100 eV, such departures affect the accuracy of established procedures for plural-scattering deconvolution, thickness measurement and Kramers-Kronig analysis. The non-dipole effect can be reduced by using an energy-dependent cutoff angle in the analysis, but it appears to amount to only a few percent and (especially for thicker specimens) may be outweighed by the effect of plural (elastic + inelastic) scattering, which is not removed by conventional deconvolution methods.

In the core-loss region of the spectrum, non-Lorentzian behaviour involves a reduction of the generalized oscillator strength from its optical value or (for energy losses much greater than an ionization threshold) a free-electron response that gives rise to a Bethe-ridge angular distribution. At incident energies above 200 keV, relativistic retardation effects distort the Lorentzian angular distribution, even for core losses just above threshold.

For the common situation of an on-axis spectrometer entrance aperture, non-dipole effects associated with higher scattering angles are largely masked, because of the rapid falloff of intensity with scattering angle. But as pointed out by Loeffler et al. (2011), off-axis measurements (e.g. of band structure or magnetic chiral dichroism) may be significantly affected, requiring more sophisticated theory for their analysis.

Near-edge fine structure can be interpreted in terms of a symmetry-projected density of states, but the dipole selection rule breaks down for higher scattering angles

and energies far above the ionization threshold. A small angle-limiting collection aperture helps to minimize this effect.

ACKNOWLEDGMENTS

The authors are grateful for financial support from the Natural Sciences and Engineering Research Council of Canada

REFERENCES

- Ahn CC, Krivanek OL. 1983. *EELS Atlas*. Gatan Inc., Warrendale, PA.
- Batson PE, Silcox J. 1983. Experimental energy-loss function, $\text{Im}[-1/\epsilon(q,\omega)]$, for aluminum. *Phys. Rev. B* 27: 5224-5239.
- Bazylev VA, Glebov, VI, Denisov, EI, Zhebago, NK, Khlebnikov, AS. 1976. Cerenkov radiation as an intense x-ray source. *JETP Lett.* 24:371-374.
- Bertoni G, Verbeeck J, Broens, F. 2011. Fitting the momentum dependent loss function in EELS. *Microsc. Res. & Technique.* 74:212-218.
- Cheng SC, Egerton RF. 1993. Elemental analysis of thick amorphous specimens by EELS. *Micron* 24:251-256.
- Cueva P, Muller DA. 2013. Atomic-scale optical and vibrational spectroscopy with low loss EELS. *Microsc. Microanal.* 19(Suppl 2):1130-1131.
- Dwyer C. 2014. Localization of high-energy electron scattering from atomic vibrations. *Phys. Rev. B* 89:054103.
- Egerton RF. 1978. K-shell ionization cross-sections for use in microanalysis. *Ultramicroscopy* 4:169-179.
- Egerton RF. 2011. *Electron Energy-Loss Spectroscopy in the Electron Microscope*, 3rd edition. Springer, New York.
- Egerton RF. 2014. Prospects for vibrational-mode EELS with high spatial resolution. *Microscopy & Microanalysis*, doi:10.1017/S1431927613014013
- Egerton RF, Wang ZL. 1990. Plural-scattering deconvolution of electron energy-loss spectra recorded with an angle-limiting aperture. *Ultramicroscopy* 32:137-148.
- Egerton RF, Wong K. 1995. Some practical consequences of the Lorentzian angular distribution of inelastic scattering. *Ultramicroscopy* 59:169-180.
- Essex DW, Nellist PD, Whelan CT. 1999. Limitations of the dipole approximation in calculations for the scanning transmission electron microscope. *Ultramicroscopy* 80:183-192.

- Ferrell, RA. 1957. Characteristic energy loss of electrons passing through metal foils: II Dispersion relation and short wavelength cutoff for plasma oscillations. *Phys. Rev.* 107:450-462.
- Inokuti M. 1971. Inelastic collisions of fast charged particles with atoms and molecules – The Bethe theory revisited. *Rev. Mod. Phys.* 43, 297-347.
- Krivanek OL, Lovejoy TC, Dellby N, Carpenter RW. (2013). Monochromated STEM with a 30 meV-wide, atom-sized electron probe. *Microscopy* 62:3–21.
- Kurata H, Wahlbring P, Isoda S, Kobayashi T. 1997. Importance of relativistic effect on inelastic scattering cross-sections for quantitative microanalysis. *Micron* 28:381-388.
- Leapman RD, Rez P, Mayers DF. 1980. K, L, and M shell generalized oscillator strengths and ionization cross sections for fast electron collisions *J. Chem. Phys.* 72:1232-1243.
- Loeffler S., Ennen I., Tian F., Schattschneider P., Jaouen N. 2011. Breakdown of the dipole approximation in core losses. *Ultramicroscopy* 111:1162-1167.
- Manson ST. 1972. Inelastic collisions of fast charged particles with atoms: Ionization of the aluminum L-shell. *Phys. Rev. A* 6, 1013-1024
- Radtke G, Botton GA, Verbeeck J. 2006. Electron inelastic scattering and anisotropy: The two-dimensional point of view. *Ultramicroscopy* 106: 1082:1900.
- Rez, P. 1989. Inner-shell spectroscopy: an atomic view. *Ultramicroscopy* 28:16-23.
- Rez, P. 2014. Is localized infra red spectroscopy now possible in the electron microscope? *Microscopy & Microanalysis*, in press.
- Saldin DK, Yao JM. 1990. Dipole approximation in electron energy-loss spectroscopy: K-shell excitations. *Phys. Rev. B* 41:52-61.
- Stoeger-Pollach M, Franco H., Schattschneider P, Lazar S, Schaffer B, Grogger BW, Zandbergen HW. 2006. Cerenkov losses: A limit for bandgap determination and Kramers–Kronig analysis. *Micron* 37:396-402.
- Souche C, Jouffrey B, Hug G, Nelhiebel M. 1998. Orientation sensitive EELS – Analysis of boron nitride nanometric hollow spheres. *Micron* 29:419-424.
- Su DS, Schattschneider P, Pongratz, P. 1992. Aperture effects and the multiple-scattering problem of fast electrons in electron energy-loss spectroscopy. *Phys. Rev. B* 46:2775-2780.
- Urban KW, Mayer J, Jinschek JR, Neish MJ, Lugg NR, Allen LJ. 2013. Achromatic elemental mapping beyond the nanoscale in the transmission electron microscope. *Phys. Rev. Lett.* 110, 185507.